The Astrophysical Journal, 893:136 (12pp), 2020 April 20 https://doi.org/10.3847/1538-4357/ab7a28

A Statistical Study of the Plasma and Composition Distribution inside Magnetic Clouds: 1998–2011

Jin Huang[1,2,3], Yu Liu[1,2,3], Hengqiang Feng[4], Ake Zhao[5], Z. Z. Abidin[6], Yuandeng Shen[1], and Oloketuyi Jacob[1,3]
[1] Yunnan Observatories, Chinese Academy of Sciences, Kunming 650216, People's Republic of China; huang_heliophysics@163.com
[2] Shandong Provincial Key Laboratory of Optical Astronomy and Solar-Terrestrial Environment, Shandong University, Weihai 264209, People's Republic of China
[3] University of Chinese Academy of Sciences, Beijing 100049, People's Republic of China; lyu@ynao.ac.cn
[4] Institute of Space Physics, Luoyang Normal University, Luoyang 471934, People's Republic of China
[5] College of Physics and Electric Information, Luoyang Normal University, Luoyang 471934, People's Republic of China
[6] Radio Cosmology Lab, Department of Physics, Faculty of Science, University of Malaya, 50603 Kuala Lumpur, Malaysia
Received 2019 November 5; revised 2020 February 19; accepted 2020 February 20; published 2020 April 23

Abstract

A comprehensive analysis of plasma and composition characteristics inside magnetic clouds (MCs) observed by the *Advanced Composition Explorer* spacecraft from 1998 February to 2011 August is presented. The results show that MCs have specific interior structures, and MCs of different speeds show differences in composition and structure. Compared with the slow MCs, fast MCs have enhanced mean charge states of iron, oxygen, silicon, magnesium, O^{7+}/O^{6+}, C^{6+}/C^{5+}, C^{6+}/C^{4+}, and $Fe^{\geqslant 16+}/Fe_{total}$ values. For ionic species in fast MCs, a higher atomic number represents a greater enhancement of mean charge state than slow MCs. We also find that both the fast and slow MCs display bimodal structure distribution in the mean iron charge state ($\langle Q\rangle$Fe), which suggests that the existence of flux rope prior to the eruption is common. Furthermore, the $\langle Q\rangle$Fe, $Fe^{\geqslant 16+}/Fe_{total}$, and O^{7+}/O^{6+} ratio distribution inside fast MCs have the feature that the posterior peak is higher than the anterior one. This result agrees with the "standard model" for coronal mass ejection/flares, by which magnetic reconnection occurs beneath the flux rope, thereby ionizing the ions of the posterior part of the flux rope sufficiently by high-energy electron collisions or by direct heating in the reconnection region.

Unified Astronomy Thesaurus concepts: Solar wind (1534); Solar coronal mass ejections (310); Interplanetary physics (827); Solar physics (1476); Solar storm (1526); Solar flares (1496); Solar filament eruptions (1981); Solar filaments (1495)

1. Introduction

Coronal mass ejections (CMEs), which are the most severe explosive phenomena in the heliosphere, observed with coronagraphs (e.g., Howard 2011; Lugaz & Roussev 2011), play a central role in the influence of the active Sun on significant interplanetary disturbances, and geospace environment variations via the solar wind (SW).

Many CMEs, for some instances, correspond to a magnetically organized geometry of flux rope (termed as flux rope CMEs; Chen 1996; Gibson & Low 1998), the occurrence of magnetic flux ropes in interplanetary space, often referred to as magnetic clouds (MCs; Burlaga et al. 1981), which have been associated with prominence eruptions at the Sun (Burlaga et al. 1982). MCs are large-scale, organized magnetic flux rope structures, characterized by several signatures, as reviewed, for example, by Gosling (1990), Neugebauer & Goldstein (1997), and Zurbuchen & Richardson (2006). We are now able to use a combination of the magnetic field, plasma, compositional, and energetic particle signatures to identify MCs. In order to provide a credible link between MCs and eruptive prominences of the Sun, in-depth exploration of the magnetic field structure and topology of MCs has been performed (e.g., Lepping et al. 1990; Bothmer & Schwenn 1998; Hu & Sonnerup 2002), and statistical studies of their internal plasma and composition have been conducted by some authors as well (e.g., Rodriguez et al. 2004; Kim et al. 2013; Owens 2018). Most of them explored the MCs' internal structure by case event studies or statistical analysis by time series.

Lynch et al. (2003, hereafter Lynch03), carried out a superposed epoch analysis to explore the internal structure of the MCs. They constructed diameter cuts through MC profiles (1998–2001) to obtain plasma and composition quantity on average, and associate the in situ measured quantity with a radial distance in the MC cylinder model. It is a good supplement to the traditional analysis of MCs. In this study, we extend the statistical period to span a solar cycle and apply this method for more desired plasma, elemental composition, especially ionic charge state quantity to seek the statistical properties of internal MCs.

The ionic charge states of plasma in a CME are an imprint of the electron temperature distribution on a few solar radii ($R_\odot$) above the solar surface, and the appearance of high ionic charge states usually implies high electron temperatures. During CME eruption, magnetic reconnection occurs along the current sheet that connects the CME flux rope structure to flare loops (Bemporad et al. 2006; Ko et al. 2013; Song et al. 2015c, 2015b), and reconnection heats the plasma, as this process continues, the heated plasma injects into the flux rope along magnetic field lines (Ko et al. 2013). On CME transits' way to the Earth, the coronal electron density continually decreases, and solar wind ion expansion time is smaller than the ionization and recombination timescales at a certain altitude. Thereafter, heavy-ion (atomic number >2) charge states and elemental composition are not apparently changed, which often happens within 5 $R_\odot$, namely, freeze-in. Therefore, such properties can be used to infer the formation time of the magnetic flux rope in MC and the current sheet temperature information during CME eruption (e.g., Ko et al. 1999; Lynch et al. 2011; Lepri et al. 2012). A high/normal ionic charge state indicates high/normal current sheet temperature (e.g., Ciaravella et al. 2013). In general, they provide not only one of the best tools to identify CME material in

interplanetary space, but also an important way to trace back the solar environment of the MCs origin (Geiss et al. 1995).

There are two theories of the origin of flux rope CMEs: (1) the flux ropes exist prior to the eruption and erupt via some mechanism; and (2) the flux rope structure was formed during the eruption. Some observations (e.g., Liu et al. 2003; Zhang et al. 2012; Cheng et al. 2013, 2014a; Patsourakos et al. 2013; Song et al. 2014) and numerical simulations (Lin & Forbes 2000) support the former, whereas other simulations (Mikic & Linker 1994) and observations (Ouyang et al. 2015) hold that flux ropes can also be formed during the eruption. Song et al. (2016) made a comprehensive survey of the mean iron charge state $\langle Q\rangle$Fe distributions inside MCs for solar cycle 23. Results showed that 11 in 92 MCs exhibited a bimodal distribution with both peaks higher than 12+ for $\langle Q\rangle$Fe. During eruption, a preexisting flux rope with relatively low temperature was surrounded by reconnecting magnetic field lines and heated plasma. When the corresponding MC was detected near the Earth, the high-ionization-state shell and the low-ionization-state center were found (Lin et al. 2004; Ko et al. 2013; Song et al. 2015a). Such a bimodal profile of $\langle Q\rangle$Fe suggests that the flux rope in MCs existed before the CMEs' eruption. It is necessary to test the scenario in a preliminary and statistical approach with in situ observations.

Another controversial issue associated with CMEs is which factors determine the CME velocity. Yashiro et al. (2002) and Vršnak et al. (2005) revealed that there is only a weak correlation between the CME apparent velocity and the peak flux of the associated flares. A different conclusion drawn by Reinard & Biesecker (2009) is that energetic source regions produce fast CMEs that are accompanied by larger flares whereas less energetic sources produce slow CMEs accompanied by smaller flares. This conclusion complies with the view that CME velocity is related to magnetic reconnection flux (Qiu & Yurchyshyn 2005) or magnetic field in the filament channel (Chen et al. 2006). In general, if CME is faster (slower) than the ambient SW, and it is decelerated (accelerated) by the SW (Chen 1996), but fast/slow MCs still correspond to fast/slow flux rope CMEs at 1 au (Lindsay et al. 1999). Therefore, in this study, we try to investigate the plasma, elemental, and charge state composition differences between the fast and the slow MCs, to improve understanding on this issue.

This study is focused on the internal structure of the plasma and ionic charge states obtained from the inherent geometry of the linear force-free magnetic field model, shedding more light on characteristic differences of fast/slow MCs by making a comprehensive survey of 124 MCs for 1998–2011 using *Advanced Composition Explorer* (*ACE*; Chiu et al. 1998) spacecraft data. The study is structured as follows: Section 2 describes data and event selection procedure, and fit the events with a linear force-free model. In Section 3, we describe the method of inferring spatial position. Section 4 presents the statistical results, followed by explanations of the results and conclusion in Section 5.

2. Data Description, Events Selection, and Model Fitting

We have identified and modeled 124 MC events observed by the *ACE* spacecraft between 1998 February and 2011 August, when *ACE*/SWICS data are available, covering a solar cycle. The magnetic field magnitude data were provided by *ACE*/MAG every 4 minutes. Helium-to-proton density ratio (He/P), SW bulk speed, and proton temperature data were provided with a cadence of 1 hr by *ACE*/SWEPAM. The rest of the data came from *ACE*/SWICS, in which O^{7+}/O^{6+}, C^{6+}/C^{5+}, C^{6+}/C^{4+}, and Fe/O, charge state of C, O, Mg, Si, and Fe used 1 hr cadence data, Ne/O, Mg/O, Si/O, C/O, and He/O used 2 hr cadence data, and proton number density used 12 minute cadence data. Descriptions of related instruments were given by Smith et al. (1998), McComas et al. (1998), and Gloeckler et al. (1998).

Our MC events come partly from *ACE* observations published in the KASI online MC list (see the cylinder model events in http://sos.kasi.re.kr/mc/). In addition, considering the scale of the MCs, there is little difference between *WIND* and *ACE* observations in most cases, thus we also tried to employ *WIND* observations as supplements. The *WIND* MC lists of Lepping et al. (2006, 2011) and Wang et al. (2016) therefore were referenced. All of the candidates were checked with *ACE* data by visual inspection according to the criterion given by Burlaga et al. (1981). Roughly enhanced magnetic field strength and relatively smooth change in field direction are required. Subsequently, they were fitted by a static, constant-α, cylindrically symmetric, force-free MC model (Burlaga 1988; Lepping et al. 1990), which is still one of the most commonly used techniques to analyze MC to date. The magnetic force-free field with constant-α satisfies Equation (1).

$$\nabla \times \boldsymbol{B} = \alpha \boldsymbol{B}. \tag{1}$$

One of the solutions of Equation (1) in the cylindrical geometry is the Lundquist solution (Lundquist 1950), in terms of axial [z], tangential [ϕ], and radial [ρ] cylindrical components,

$$B_\rho = 0, \qquad B_\phi = HB_0J_1(\alpha\rho), \qquad B_Z = B_0J_0(\alpha\rho), \tag{2}$$

where B_0 is the field magnitude on the cylinder axis, ρ is the distance from the axis, H is the sign of the helicity, and J_0, and J_1 are zeroth- and first-order Bessel functions, respectively. The constant value of α is derived from the radius of the cloud model cylinder (R_c), such that their product is the first zero of J_0. The fitting procedure described by Lepping et al. (1990) was applied to the analysis. The candidate events' possible boundaries were tested and chosen only when the boundaries were close to the best-fit boundaries and the fitting results were reasonably acceptable, i.e., normalized rms $\chi_n < 0.6$ (Wang et al. 2018) and the closest distance of the spacecraft to the rope axis (d), namely impact parameter, in units of R_c, satisfies $d \leqslant 0.8$. Finally, 64 *ACE* and 60 *WIND* observation events were selected. Table 1 lists the model fit parameters. Histograms of some fundamental parameters [$\triangle t$, $V_{\rm rad}$, R_c, B_0, θ, ϕ, d, χ_n] are displayed in Figure 1. Definitions are given in the caption of Table 1. As shown by Figure 1, faster MCs have larger B_0 than slow ones. Moreover, our χ_n and d tend to be large, but they are still within a reasonable range.

Comparing the events' boundaries with Lynch03's, we found that 24/56 events have overlaps, but none of them are identical, which should cause the fitting parameters to have clear differences. We also compared our fitting results with KASI and Lepping et al. (2006), whose boundaries are the same as ours. As listed in Table 2, taking the events in 1998 as an example, most of the results can approximate theirs well.

Table 1
ACE MC Events and Model Fit Parameters

No.	Shock Start	MC Start	MC End	Δt (hr)	$V_{\rm rad}$ (km s^{-1})	d ($1/R_c$)	t_c	B_0 (nT)	R_c (au)	θ (deg)	ϕ (deg)	H	χ_n
1	1998 May 1 21:22:45	1998 May 2 12:18:00	1998 May 3 17:18:00	29.0	517	0.65	1998 May 3 02:48:28	9.06	0.112	27.06	7.83	−1	0.52
2	…	1998 May 5 13:00:00	1998 May 6 00:00:00	11.0	566	0.22	1998 May 5 18:29:32	8.86	0.050	6.11	319.35	1	0.40
3	1998 Jun 23 07:10:00	1998 Jun 24 16:48:00	1998 Jun 25 21:48:00	29.0	456	0.40	1998 Jun 25 7:18:30	15.70	0.059	16.63	169.35	−1	0.37
4	1998 Sep 24 23:13:24	1998 Sep 25 10:18:00	1998 Sep 26 13:18:00	27.0	627	0.55	1998 Sep 25 23:48:28	15.64	0.205	52.27	206.60	−1	0.36
5	1998 Nov 7 07:36:46	1998 Nov 8 23:48:00	1998 Nov 10 01:18:00	25.5	451	0.07	1998 Nov 9 12:33:26	16.39	0.133	−72.85	10.25	1	0.41
6	…	1999 Apr 21 12:00:00	1999 Apr 22 14:00:00	26.0	479	0.70	1999 Apr 22 00:59:30	11.37	0.132	−4.33	39.08	−1	0.37
7	1999 Jul 2 00:23:00	1999 Jul 3 07:15:00	1999 Jul 3 22:15:00	15.0	522	0.78	1999 Jul 3 14:45:29	7.35	0.140	43.12	58.56	−1	0.28
8	…	1999 Aug 1 03:00:00	1999 Aug 2 11:00:00	32.0	469	0.76	1999 Aug 1 18:59:33	7.38	0.267	20.25	286.48	−1	0.38
9	1999 Nov 13 12:13:00	1999 Nov 14 01:00:00	1999 Nov 14 09:00:00	8.0	443	0.74	1999 Nov 14 05:00:24	10.80	0.050	16.47	129.49	1	0.40
10	2000 Feb 11 23:18:00	2000 Feb 12 12:00:00	2000 Feb 13 00:00:00	12.0	542	0.40	2000 Feb 12 18:00:31	13.79	0.045	31.65	181.47	1	0.47
11	2000 Jul 11 11:23:00	2000 Jul 11 22:30:00	2000 Jul 13 04:30:00	30.0	507	0.78	2000 Jul 12 13:29:31	14.52	0.270	50.77	52.51	−1	0.40
12	2000 Jul 28 05:42:00	2000 Jul 28 21:06:00	2000 Jul 29 10:06:00	13.0	463	0.68	2000 Jul 29 03:36:27	16.66	0.009	2.63	4.23	1	0.53
13	2000 Aug 11 18:11:00	2000 Aug 12 06:06:00	2000 Aug 13 05:06:00	23.0	550	0.04	2000 Aug 12 17:36:24	24.83	0.151	25.98	99.83	−1	0.44
14	2000 Nov 6 09:14:00	2000 Nov 623:06:00	2000 Nov 7 18:06:00	19.0	532	0.44	2000 Nov 7 08:36:28	27.14	0.089	9.73	140.01	−1	0.24
15	2001 Mar 3 10:39:00	2001 Mar 4 15:30:00	2001 Mar 5 01:30:00	10.0	437	0.66	2001 Mar 4 20:29:35	12.75	0.049	−44.73	183.88	1	0.41
16	2001 Mar 27 17:15:00	2001 Mar 27 21:45:00	2001 Mar 28 06:00:00	8.3	613	0.73	2001 Mar 28 01:52:27	19.85	0.036	−14.11	199.24	1	0.25
17	…	2001 Apr 1 05:00:00	2001 Apr 1 20:00:00	15.0	767	0.53	2001 Apr 1 12:29:31	8.48	0.128	51.22	172.36	−1	0.40
18	2001 Apr 28 04:31:00	2001 Apr 29 01:54:00	2001 Apr 29 12:54:00	11.0	636	0.56	2001 Apr 29 07:23:34	13.42	0.102	13.18	93.74	−1	0.22
19	2001 May 8 09:31:00	2001 May 9 12:00:00	2001 May 10 21:00:00	33.0	435	0.73	2001 May 10 04:30:30	11.06	0.055	9.01	8.74	−1	0.36
20	2001 May 27 14:18:00	2001 May 28 11:54:00	2001 May 29 10:24:00	22.5	455	0.63	2001 May 28 23:09:24	13.25	0.063	−6.72	22.38	−1	0.34
21	2002 Mar 23 10:53:00	2002 Mar 24 03:48:00	2002 Mar 25 22:48:00	43.0	435	0.12	2002 Mar 25 01:17:33	15.88	0.223	36.25	283.59	1	0.40
22	2002 Apr 17 10:21:00	2002 Apr 18 01:00:00	2002 Apr 19 10:00:00	33.0	474	0.73	2002 Apr 18 17:29:30	17.95	0.115	−6.79	336.09	1	0.32
23	2002 Apr 19 08:02:00	2002 Apr 20 11:48:00	2002 Apr 21 16:48:00	29.0	516	0.63	2002 Apr 21 02:17:31	9.25	0.020	1.13	85.05	1	0.38
24	2002 Aug 1 04:24:00	2002 Aug 1 11:54:00	2002 Aug 1 22:36:00	10.7	458	0.63	2002 Aug 1 17:15:24	15.59	0.067	13.54	299.65	1	0.42
25	2002 Aug 1 22:19:00	2002 Aug 2 04:15:00	2002 Aug 2 20:15:00	16.0	494	0.79	2002 Aug 2 12:15:24	19.47	0.030	2.78	169.49	1	0.24
26	…	2002 Aug 20 15:00:00	2002 Aug 21 12:00:00	21.0	453	0.72	2002 Aug 21 01:29:30	12.59	0.043	−14.24	174.30	−1	0.34
27	…	2003 Mar 31 04:00:00	2003 Mar 31 13:00:00	9.0	581	0.27	2003 Mar 31 08:29:29	11.51	0.064	−3.52	258.30	−1	0.50
28	…	2003 Jun 17 17:48:00	2003 Jun 18 08:18:00	14.5	490	0.72	2003 Jun 18 01:03:27	16.17	0.057	−9.06	206.15	−1	0.43
29	…	2003 Aug 5 09:30:00	2003 Aug 6 01:00:00	15.5	431	0.65	2003 Aug 5 17:14:32	13.84	0.101	13.85	251.98	−1	0.34
30	…	2003 Aug 16 10:30:00	2003 Aug 17 14:30:00	28.0	492	0.79	2003 Aug 17 00:30:30	9.71	0.100	−5.16	21.05	−1	0.36
31	2003 Aug 17 13:41:00	2003 Aug 18 10:30:00	2003 Aug 19 15:30:00	29.0	436	0.08	2003 Aug 19 00:59:34	19.20	0.120	−12.22	309.31	1	0.45
32	2003 Oct 30 16:18:00	2003 Oct 31 02:30:00	2003 Nov 1 00:30:00	22.0	1028	0.72	2003 Oct 31 13:29:32	15.87	0.366	30.61	245.38	−1	0.50
33	2003 Nov 20 07:27:00	2003 Nov 20 10:48:00	2003 Nov 21 02:18:00	15.5	581	0.10	2003 Nov 20 18:33:29	28.01	0.108	−64.45	248.37	1	0.58
34	2004 Jan 9 14:51:00	2004 Jan 10 10:15:00	2004 Jan 10 18:00:00	7.8	539	0.76	2004 Jan 10 14:07:30	16.46	0.046	−5.01	216.43	−1	0.33
35	2004 Apr 3 09:00:45	2004 Apr 4 02:48:00	2004 Apr 5 14:48:00	36.0	434	0.52	2004 Apr 4 20:47:35	20.22	0.218	79.36	227.41	−1	0.44
36	2004 Jul 22 09:55:00	2004 Jul 22 15:24:00	2004 Jul 22 23:06:00	7.7	602	0.44	2004 Jul 22 19:15:28	19.17	0.047	−22.27	45.71	1	0.55
37	2004 Jul 24 05:45:24	2004 Jul 24 12:48:00	2004 Jul 25 13:18:00	24.5	560	0.37	2004 Jul 25 01:02:31	24.87	0.173	−38.50	72.49	1	0.32
38	2004 Jul 26 22:28:00	2004 Jul 27 01:50:00	2004 Jul 27 15:20:00	13.5	916	0.05	2004 Jul 27 08:34:31	25.36	0.145	−23.13	105.33	1	0.39
39	2004 Nov 7 17:51:00	2004 Nov 8 03:24:00	2004 Nov 8 16:36:00	13.2	667	0.28	2004 Nov 8 10:00:24	15.94	0.076	0.91	43.49	−1	0.43
40	2004 Nov 9 18:21:00	2004 Nov 9 20:54:00	2004 Nov 10 03:24:00	6.5	805	0.49	2004 Nov 10 00:09:28	45.15	0.059	17.37	307.14	−1	0.39
41	2005 May 15 02:11:00	2005 May 15 05:30:00	2005 May 16 12:30:00	31.0	820	0.51	2005 May 15 17:00:30	31.87	0.219	54.85	210.51	−1	0.47
42	2005 May 20 03:37:45	2005 May 20 07:18:00	2005 May 21 05:18:00	22.0	457	0.12	2005 May 20 18:17:34	12.17	0.122	60.36	272.74	−1	0.58
43	2005 Jun 12 06:52:30	2005 Jun 12 15:36:00	2005 Jun 13 07:06:00	15.5	469	0.78	2005 Jun 12 23:21:30	21.98	0.053	−19.32	11.39	−1	0.38
44	…	2005 Jun 15 23:30:00	2005 Jun 16 08:30:00	9.0	455	0.79	2005 Jun 16 04:00:26	14.12	0.057	45.04	173.97	−1	0.35
45	2005 Jul 16 01:50:30	2005 Jul 17 15:18:00	2005 Jul 18 03:48:00	12.5	426	0.49	2005 Jul 17 21:33:25	15.13	0.073	−30.66	99.54	1	0.34
46	2005 Sep 2 13:32:00	2005 Sep 2 19:20:00	2005 Sep 3 04:00:00	8.7	645	0.67	2005 Sep 2 23:40:30	11.27	0.052	−0.64	215.09	−1	0.48
47	…	2005 Dec 31 14:48:00	2006 Jan 1 10:48:00	20.0	465	0.70	2006 Jan 1 00:48:29	11.61	0.028	1.79	349.93	1	0.33
48	2006 Apr 13 11:12:30	2006 Apr 13 14:48:00	2006 Apr 13 20:48:00	6.0	531	0.51	2006 Apr 13 17:48:31	21.34	0.040	62.67	16.66	−1	0.36

Table 1
(Continued)

No.	Shock Start	MC Start	MC End	Δt (hr)	$V_{\rm rad}$ (km s^{-1})	d ($1/R_c$)	t_c	B_0 (nT)	R_c (au)	θ (deg)	ϕ (deg)	H	χ_n
49	⋯	2007 May 21 22:54:00	2007 May 22 13:36:00	14.7	453	0.00	2007 May 22 06:14:28	11.53	0.069	47.20	41.69	1	0.39
50	⋯	2007 Nov 19 23:20:00	2007 Nov 20 09:20:00	10.0	463	0.65	2007 Nov 20 04:19:34	24.51	0.065	3.71	241.14	−1	0.34
51	⋯	2008 Mar 8 19:20:00	2008 Mar 9 00:50:00	5.5	448	0.71	2008 Mar 8 22:05:26	14.14	0.040	−0.08	108.78	1	0.33
52	⋯	2008 May 23 02:40:00	2008 May 23 09:40:00	7.0	492	0.79	2008 May 23 06:09:31	8.55	0.065	35.08	109.87	1	0.27
53	⋯	2008 Sep 3 17:45:00	2008 Sep 4 01:15:00	7.5	464	0.65	2008 Sep 3 21:29:31	16.66	0.050	15.77	115.55	1	0.32
54	2010 Aug 3 17:00:00	2010 Aug 4 04:00:00	2010 Aug 4 08:00:00	4.0	565	0.53	2010 Aug 4 05:59:28	20.70	0.012	13.58	197.28	1	0.36
55	2011 Jun 4 19:58:00	2011 Jun 5 01:20:00	2011 Jun 5 06:26:00	5.1	500	0.77	2011 Jun 5 03:52:32	26.17	0.022	23.84	347.62	1	0.42
56	⋯	1998 Feb 4 04:30:00	1998 Feb 5 22:30:00	42.0	322	0.57	1998 Feb 5 1:30:31	12.89	0.113	9.81	33.55	−1	0.42
57	⋯	1998 Feb 17 09:30:00	1998 Feb 17 20:30:00	11.0	402	0.52	1998 Feb 17 14:59:33	14.85	0.022	−13.46	164.46	1	0.45
58	1998 Mar 4 10:58:00	1998 Mar 4 14:18:00	1998 Mar 6 06:18:00	40.0	338	0.27	1998 Mar 5 10:18:28	12.67	0.109	17.01	143.04	−1	0.32
59	1998 Jun 2 08:13:00	1998 Jun 2 10:36:00	1998 Jun 2 15:54:00	5.3	409	0.73	1998 Jun 2 13:14:33	16.51	0.010	−15.61	13.47	−1	0.27
60	⋯	1998 Jul 13 12:00:00	1998 Jul 13 19:00:00	7.0	355	0.71	1998 Jul 13 15:30:29	6.75	0.042	−63.04	83.98	1	0.43
61	1998 Aug 19 17:31:00	1998 Aug 20 10:18:00	1998 Aug 21 19:18:00	33.0	328	0.15	1998 Aug 21 02:47:28	13.51	0.128	13.11	284.16	1	0.52
62	⋯	1998 Nov 6 01:00:00	1998 Nov 6 08:00:00	7.0	403	0.80	1998 Nov 6 04:30:30	12.97	0.025	−16.04	158.17	1	0.36
63	⋯	1999 Feb 2 02:30:00	1999 Feb 2 18:30:00	16.0	288	0.77	1999 Feb 2 10:29:32	4.00	0.041	−21.41	198.13	1	0.37
64	1999 Apr 16 10:53:00	1999 Apr 16 20:18:00	1999 Apr 17 21:18:00	25.0	412	0.12	1999 Apr 17 08:47:30	15.99	0.101	−28.42	132.23	−1	0.59
65	⋯	1999 May 29 22:00:00	1999 May 30 05:00:00	7.0	390	0.78	1999 May 30 01:29:33	9.45	0.031	16.76	147.02	−1	0.34
66	1999 Jun 26 02:17:00	1999 Jun 26 06:00:00	1999 Jun 26 22:00:00	16.0	348	0.77	1999 Jun 26 14:00:26	21.44	0.012	0.84	173.67	−1	0.40
67	1999 Aug 8 17:44:00	1999 Aug 9 10:48:00	1999 Aug 10 15:48:00	29.0	338	0.50	1999 Aug 10 01:18:28	12.46	0.134	78.57	33.67	−1	0.39
68	1999 Sep 21 11:58:00	1999 Sep 21 21:06:00	1999 Sep 22 05:06:00	8.0	356	0.66	1999 Sep 22 01:05:34	17.47	0.043	6.37	72.06	−1	0.29
69	⋯	1999 Nov 21 6:20:00	1999 Nov 21 15:00:00	8.7	382	0.78	1999 Nov 21 10:39:35	14.99	0.052	1.19	235.05	1	0.27
70	⋯	2000 Jan 27 08:15:00	2000 Jan 27 14:15:00	6.0	337	0.74	2000 Jan 27 11:15:28	19.43	0.019	−15.90	26.90	−1	0.33
71	2000 Feb 20 20:44	2000 Feb 21 09:48:00	2000 Feb 22 13:18:00	27.5	385	0.33	2000 Feb 21 23:32:29	17.23	0.135	85.92	249.40	1	0.45
72	⋯	2000 May 7 18:00:00	2000 May 8 12:00:00	18.0	374	0.77	2000 May 8 02:59:32	19.34	0.114	62.35	186.05	−1	0.28
73	⋯	2000 May 12 03:20:00	2000 May 12 15:20:00	12.0	304	0.68	2000 May 12 09:20:28	11.17	0.001	−0.51	360.28	−1	0.38
74	⋯	2000 Jul 1 07:20:00	2000 Jul 2 01:20:00	18.0	412	0.72	2000 Jul 1 16:20:30	12.28	0.119	66.28	178.15	−1	0.31
75	⋯	2000 Aug 9 11:45:00	2000 Aug 9 20:30:00	8.8	373	0.10	2000 Aug 9 16:07:29	7.25	0.027	22.57	141.95	1	0.32
76	2000 Oct 3 00:08:00	2000 Oct 3 17:06:00	2000 Oct 4 14:06:00	21.0	399	0.05	2000 Oct 4 03:35:30	18.64	0.083	21.46	52.22	1	0.28
77	⋯	2000 Oct 6 20:30:00	2000 Oct 7 06:30:00	10.0	416	0.70	2000 Oct 7 01:30:25	6.38	0.041	−3.23	323.84	−1	0.26
78	2000 Oct 12 21:43	2000 Oct 13 18:24:00	2000 Oct 14 16:54:00	22.5	395	0.72	2000 Oct 14 05:39:28	18.28	0.121	−35.16	40.90	1	0.32
79	⋯	2001 Jan 19 20:50:00	2001 Jan 20 04:10:00	7.3	319	0.79	2001 Jan 20 00:30:28	5.98	0.009	3.72	191.22	1	0.34
80	⋯	2001 Jan 21 03:00:00	2001 Jan 21 13:00:00	10.0	309	0.72	2001 Jan 21 07:59:32	14.63	0.028	−24.36	159.07	1	0.34
81	2001 Mar 19 10:24:00	2001 Mar 19 23:18:00	2001 Mar 20 18:18:00	19.0	405	0.55	2001 Mar 20 08:48:28	25.07	0.032	−15.26	187.10	−1	0.22
82	2001 Apr 21 15:06:00	2001 Apr 22 00:54:00	2001 Apr 23 01:24:00	24.5	357	0.53	2001 Apr 22 13:09:28	15.24	0.078	−35.03	299.28	−1	0.32
83	⋯	2001 Jul 10 17:18:00	2001 Jul 12 08:48:00	39.5	352	0.26	2001 Jul 11 13:03:26	8.10	0.135	22.32	227.62	1	0.57
84	⋯	2001 Sep 1 21:00:00	2001 Sep 2 18:00:00	21.0	347	0.63	2001 Sep 2 07:29:28	7.45	0.080	0.51	225.39	−1	0.32
85	2001 Oct 31 12:53:00	2001 Oct 31 21:18:00	2001 Nov 2 10:18:00	37.0	332	0.01	2001 Nov 1 15:47:28	11.50	0.141	4.33	71.88	−1	0.43
86	⋯	2002 Apr 5 01:00:00	2002 Apr 5 09:00:00	8.0	416	0.57	2002 Apr 5 05:00:27	6.20	0.041	24.26	53.46	−1	0.47
87	⋯	2002 Sep 3 00:18:00	2002 Sep 3 18:48:00	18.5	352	0.55	2002 Sep 3 09:33:24	13.55	0.049	58.53	196.36	1	0.49
88	⋯	2002 Sep 29 02:00:00	2002 Sep 29 16:00:00	14.0	294	0.73	2002 Sep 29 08:59:29	18.15	0.005	3.51	178.46	1	0.31
89	2002 Sep 30 07:22:00	2002 Sep 30 22:36:00	2002 Oct 1 11:54:00	13.3	379	0.31	2002 Oct 1 05:15:29	26.52	0.038	13.71	146.35	1	0.33
90	2004 Aug 29 09:19:00	2004 Aug 29 18:42:00	2004 Aug 30 20:48:00	26.1	391	0.56	2004 Aug 30 07:44:34	15.95	0.146	−18.88	101.54	1	0.34
91	⋯	2005 Jun 22 11:30:00	2005 Jun 22 20:30:00	9.0	309	0.72	2005 Jun 22 16:00:25	10.78	0.007	−1.42	46.21	1	0.26
92	⋯	2005 Aug 11 15:30:00	2005 Aug 12 01:00:00	9.5	376	0.80	2005 Aug 11 20:15:29	7.55	0.061	14.90	57.54	1	0.23
93	2005 Aug 31 00:08:00	2005 Aug 31 10:00:00	2005 Aug 31 18:00:00	8.0	392	0.13	2005 Aug 31 14:00:30	19.05	0.038	−39.16	85.80	1	0.40
94	⋯	2005 Oct 31 02:54:00	2005 Oct 31 20:24:00	17.5	365	0.07	2005 Oct 31 11:38:30	11.42	0.052	−16.02	140.34	1	0.43
95	⋯	2006 Jan 10 05:30:00	2006 Jan 10 21:00:00	15.5	286	0.71	2006 Jan 10 13:15:24	8.16	0.061	−12.89	51.68	1	0.38
96	⋯	2006 Feb 5 21:00:00	2006 Feb 6 11:00:00	14.0	336	0.72	2006 Feb 6 04:00:24	15.52	0.034	−13.02	158.98	1	0.32

Table 1
(Continued)

No.	Shock Start	MC Start	MC End	Δt (hr)	$V_{\rm rad}$ (km s^{-1})	d ($1/R_c$)	t_c	B_0 (nT)	R_c (au)	θ (deg)	ϕ (deg)	H	χ_n
97	⋯	2006 Jul 16 02:15:00	2006 Jul 16 10:30:00	8.3	384	0.77	2006 Jul 16 06:22:25	4.84	0.051	−5.27	58.81	−1	0.38
98	⋯	2006 Jul 23 00:00:00	2006 Jul 23 22:30:00	22.5	310	0.27	2006 Jul 23 11:15:28	4.70	0.062	−27.39	322.20	1	0.46
99	2006 Aug 30 20:53	2006 Aug 30 21:06:00	2006 Aug 31 14:54:00	17.8	398	0.49	2006 Aug 31 06:00:26	10.14	0.068	−5.66	224.27	−1	0.30
100	⋯	2006 Nov 29 09:00:00	2006 Nov 30 06:00:00	21.0	419	0.15	2006 Nov 29 19:29:33	14.44	0.101	18.11	69.76	1	0.33
101	⋯	2007 Jan 14 14:06:00	2007 Jan 15 06:54:00	16.8	350	0.68	2007 Jan 14 22:30:31	17.23	0.091	8.22	249.86	−1	0.35
102	⋯	2007 Jan 26 12:00:00	2007 Jan 26 20:30:00	8.5	315	0.28	2007 Jan 26 16:14:29	3.96	0.022	37.12	342.27	−1	0.50
103	⋯	2007 Mar 24 03:06:00	2007 Mar 24 16:54:00	13.8	360	0.10	2007 Mar 24 10:00:29	9.14	0.057	−9.01	251.90	1	0.51
104	⋯	2007 Jun 6 15:40:00	2007 Jun 7 01:20:00	9.7	341	0.78	2007 Jun 6 20:30:26	4.64	0.064	−65.66	84.87	1	0.33
105	⋯	2007 Oct 9 15:00:00	2007 Oct 9 22:00:00	7.0	279	0.72	2007 Oct 9 18:29:33	2.23	0.022	39.62	28.51	−1	0.45
106	⋯	2008 Jun 12 20:00:00	2008 Jun 13 03:00:00	7.0	307	0.79	2008 Jun 12 23:29:28	5.52	0.042	−37.31	265.14	1	0.31
107	⋯	2008 Sep 1 11:00:00	2008 Sep 1 18:00:00	7.0	348	0.75	2008 Sep 1 14:29:32	4.85	0.044	−6.61	80.21	1	0.42
108	⋯	2008 Sep 17 04:00:00	2008 Sep 18 08:00:00	28.0	409	0.29	2008 Sep 17 18:00:25	6.75	0.128	59.62	24.88	1	0.36
109	2008 Dec 16 10:01:00	2008 Dec 17 03:06:00	2008 Dec 17 14:24:00	11.3	337	0.77	2008 Dec 17 08:45:31	13.36	0.018	−2.69	194.48	−1	0.23
110	⋯	2008 Dec 20 18:15:00	2008 Dec 21 02:45:00	8.5	336	0.70	2008 Dec 20 22:29:31	7.55	0.009	−3.05	189.78	−1	0.38
111	⋯	2008 Dec 22 07:30:00	2008 Dec 22 15:00:00	7.5	303	0.57	2008 Dec 22 11:14:34	8.85	0.012	13.67	343.32	−1	0.35
112	2009 Feb 3 19:08:00	2009 Feb 4 00:06:00	2009 Feb 4 10:54:00	10.8	366	0.67	2009 Feb 4 05:30:27	14.12	0.037	1.30	35.40	1	0.45
113	⋯	2009 Mar 12 00:42:00	2009 Mar 13 00:42:00	24.0	361	0.15	2009 Mar 12 12:41:34	11.24	0.105	51.73	100.88	1	0.50
114	⋯	2009 Sep 10 10:24:00	2009 Sep 10 16:24:00	6.0	306	0.74	2009 Sep 10 13:23:30	8.20	0.017	37.51	152.84	1	0.30
115	⋯	2009 Sep 11 01:30:00	2009 Sep 11 13:30:00	12.0	292	0.79	2009 Sep 11 07:30:26	8.88	0.037	−5.38	32.13	1	0.29
116	⋯	2009 Sep 29 15:15:00	2009 Sep 29 22:15:00	7.0	305	0.79	2009 Sep 29 18:44:31	4.87	0.030	−7.65	224.69	−1	0.36
117	⋯	2009 Sep 30 07:54:00	2009 Sep 30 16:54:00	9.0	348	0.75	2009 Sep 30 12:24:31	13.25	0.042	22.48	223.00	−1	0.25
118	⋯	2009 Oct 12 12:06:00	2009 Oct 12 16:54:00	4.8	363	0.80	2009 Oct 12 14:29:33	9.98	0.015	9.22	203.27	−1	0.18
119	⋯	2009 Oct 17 22:06:00	2009 Oct 18 07:24:00	9.3	316	0.75	2009 Oct 18 02:44:28	5.13	0.047	12.37	118.40	1	0.28
120	⋯	2009 Oct 29 05:12:00	2009 Oct 29 22:48:00	17.6	367	0.70	2009 Oct 29 14:00:26	13.55	0.035	3.06	263.21	−1	0.40
121	⋯	2009 Nov 2 02:15:00	2009 Nov 2 10:15:00	8.0	320	0.80	2009 Nov 2 06:14:34	11.36	0.018	−3.62	200.64	−1	0.29
122	⋯	2009 Dec 12 19:48:00	2009 Dec 14 05:18:00	33.5	266	0.76	2009 Dec 13 12:32:35	8.83	0.087	−1.91	31.80	1	0.40
123	2010 May 28 02:02:00	2010 May 28 19:50:00	2010 May 29 15:02:00	19.2	355	0.47	2010 May 29 05:25:30	17.73	0.057	−32.42	201.02	−1	0.31
124	2011 Mar 29 15:00:00	2011 Mar 30 00:35:00	2011 Mar 31 07:23:00	30.8	342	0.61	2011 Mar 30 15:58:35	17.02	0.147	40.28	58.69	1	0.33

Parameters of the MCs Involved in the Study

Parameter	Explanation
$\triangle t$	Duration of the MC interval.
$V_{\rm rad}$	MC averaged radial velocity.
d	Impact parameter, in units of R.
t_c	The time when the spacecraft arrives at the closest approach.
B_0	Magnetic field strength at the axis of the MFR.
R_c	The radius of the MC, in units of au.
θ	Elevation angle of the axis of the MFR in GSE coordinates.
ϕ	Azimuthal angle of the axis of the MFR in GSE coordinates.
H	Handedness or sign of helicity, set to 1 (right) or −1 (left).
χ_n	Normalized rms of the difference between the modeled results and observed data.

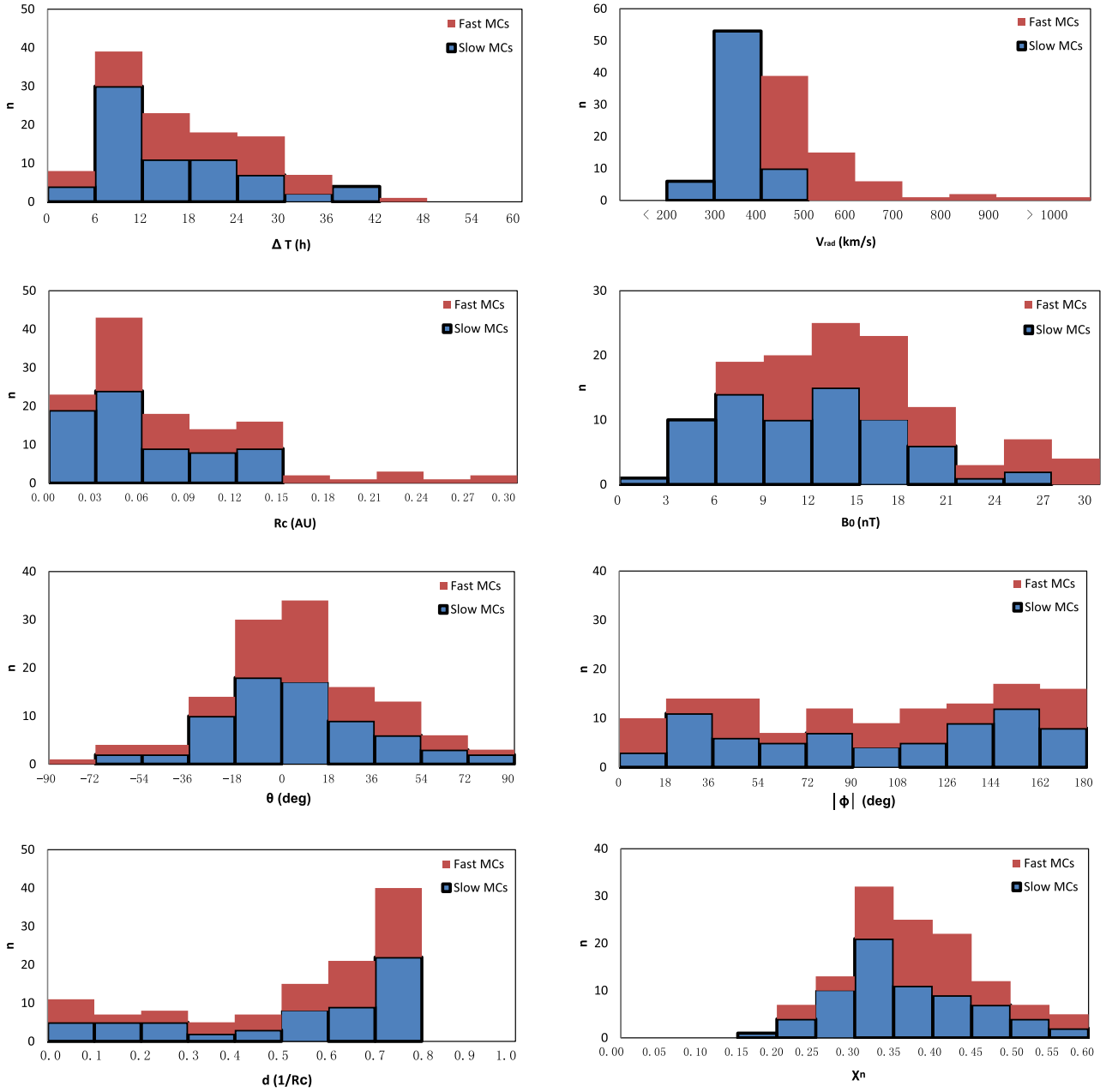

Figure 1. Histogram distributions of MCs' fit parameters. The red bars indicate fast MCs, the thick outlined bars in blue represent slow MCs.

3. Method of Inferring Spatial Position

We used Lynch03's method (note that bins defined have some changes) to extract composition spatial structure from the magnetic field model. As shown in Figure 2, the green arrows indicate the spacecraft trajectory and direction, and the circular region represents the MC cross-section. This figure describes the trajectory of the spacecraft in the cloud projected onto the plane perpendicular to the cloud axis. The *ACE* measured quantity has been coupled with the radial distance inside the model cylinder using the model geometry. We define x as the normalized spatial position of the measured quantity.

$$x = \frac{|\mathrm{OA}|}{|\mathrm{OB}|} \tag{3}$$

In Equation (3), |OB| is R_c, and |OA| can be easily calculated by |AB| (determined by *ACE* traveling time segment and flow velocity), |OB|, and |OC| (that is d). Note that the distances |OA| are symmetric around the |OC| of the model fit. By applying this procedure, we can obtain the common MC structure among different sizes, and construct the statistical average of any measured quantity.

4. Results

In this paper, we made a comprehensive survey of the plasma and composition distributions inside 124 MCs during 1998 February–2011 August. MCs have an average SW speed of 420 km s^{-1} near 1 au (Klein & Burlaga 1982). Therefore, we classified the MCs into fast (55 MCs) and slow (69 MCs) types with a threshold of 420 km s^{-1}. After inferring the corresponding x value of every measured quantity as Section 3, we divided the x values into 11 bins, calculated the mean value in each bin, and let error bars denote standard error of the

Table 2
Parameter Comparison between Our Results and the Other Studies

Spacecraft		MC Interval		B_0 (nT)	θ (deg)	ϕ (deg)
		Begin	End			
ACE	KASI	1998 Feb 17 09:30	1998 Feb 17 20:30	14.0	−9.0	173.8
	Our results			14.9	−13.5	164.5
	KASI	1998 May 5 13:00	1998 May 6 00:00	9.0	7.3	309.2
	Our results			8.9	6.1	319.4
	KASI	1998 Jul 13 12:00	1998 Jul 13 19:00	7.0	−54.6	76.2
	Our results			6.7	−63.0	84.0
WIND	Lepping	1998 Jun 24 16:48	1998 Jun 25 21:48	15.5	21.0	151.0
ACE	Our results			15.7	16.6	169.3
WIND	Lepping	1998 Aug 20 10:18	1998 Aug 21 19:18	16.6	18.0	287.0
ACE	Our results			13.5	13.1	284.2
WIND	Lepping	1998 Sep 25 10:18	1998 Sep 26 13:18	18.5	46.0	212.0
ACE	Our results			15.6	52.3	206.6

quantities within the bins. If the *ACE* spacecraft passes through MC along the green arrow in Figure 2, the quantity distributions inside MCs (Figure 3) will be detected. The positive x-axis is the sunward side, whereas the negative x-axis is the earthward side. To compare with ambient SW status, SW mean value was calculated for all quantities. If there is a leading shock preceding MC, the calculated period is 12 hr before the leading shock, otherwise, the period is 16–4 hr before the leading edge of MCs. Four hours ahead of MCs here is to avoid the errors in MC boundary selections. All the times of the shocks and MC boundaries are shown with respect to *ACE* time. Results of all quantity distributions inside MCs are shown in Figure 3; the related comments are as follows:

(a) Magnetic field magnitude ($|B|$). Both fast and slow MCs show a domed-like profile. The fast MCs' profile is much higher and smoother than the slow MCs'. The slow MCs' profile is roughly symmetric about the midpoint, while the forward part of fast MCs is clearly higher than their rear part, which can be explained by the compression of upstream SW and violent radial expansion (Osherovich et al. 1993). In addition, the leading edge bin (span −1.0 to −0.9) of the fast MCs shows a notable rise, the similar phenomenon is also found at proton temperature (panel (b)) and proton density distributions (panel (d)). The reason may be that there are some

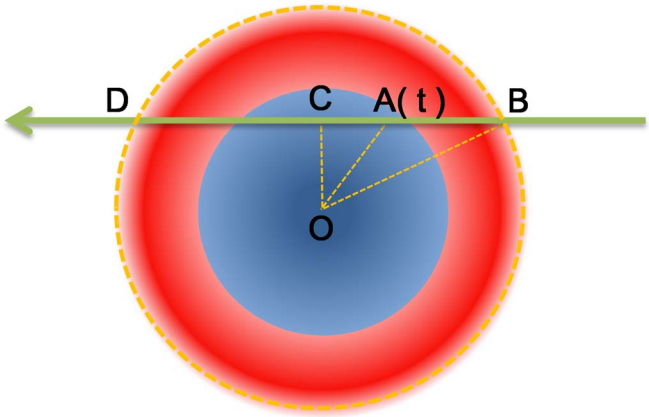

Figure 2. Schematic drawing of the *ACE* spacecraft trajectory in the MC frame, showing the positions of a measured quantity during the MC event and the explanation of bimodal distributions of $\langle Q \rangle$Fe inside the MC. The orange dotted circle marks the boundary of the MC, the green arrow is *ACE* trajectory, $A(t)$ is the measured quantity position, and red/blue denotes the high/low $\langle Q \rangle$Fe region.

deviations in MC boundary determinations, thus the leading edges of fast MCs are mixed with contaminations from the ICME sheaths, which were typically generated by fast MCs.

(b) Proton temperature (T_p). Compared with the slow MCs, fast MCs show higher T_p, and much hotter edges, which could result from the interaction with the ambient SW (Gosling et al. 2007) or the other ICMEs (Lugaz et al. 2005).

(c) Radial velocity of SW ($V_{\rm rad}$). As a result of severe and fluctuant expansion, it shows an uneven decrease throughout fast MCs, while the slight and smooth decline of slow MCs is consistent with their mild and steady expansion. The former is faster than the upstream SW, while the latter is about the same as the upstream SW at 1 au. Also, there is a protrusion in the center of fast MCs, the same signature can be seen in Figure 9 of Lynch03.

(d) Proton density (N_p). Contrary to T_p, fast MCs have lower N_p than slow MCs. Both fast and slow MCs appear almost symmetric (coinciding with the result of Lynch03) and denser center profiles, agree with the three-part CME structure. Besides, the N_p of fast MCs is almost at the same level as the upstream SW.

(e) He/P ratio. Both fast and slow MCs tend to increase from the leading to the trailing edge; this trend also appears in Figure 9 of Lynch03. In addition, many previous studies suggested that most of the ICMEs have high He/P. For instance, Richardson & Cane (2004) used the criterion of He/P $>$ 0.06 that are typically associated with ICMEs, Burlaga et al. (2001) and Elliott et al. (2005) identified ICMEs with the criterion of He/P $>$ 0.08. As a subset of ICMEs, in our statistics, fast MCs are almost equal to 0.06, while slow MCs are lower than this criterion on average. It seems that the He/P ratio tends to be depleted if the ICME has MC structure. In comparison to corresponding SW, both fast and slow MCs show a higher He/P ratio, which may be a consequence of reconnection-driven currents leading to chromospheric evaporation at the footpoints of the loops during CME eruption (Zurbuchen et al. 2003).

(f) $\langle Q \rangle$Fe. It is straightforward to analyze Fe charge states due to its large mass and high abundance in the solar wind. What's more, contrasting to C and O ions, which are easily affected by heating processes at the earlier stage, Fe ions freeze-in

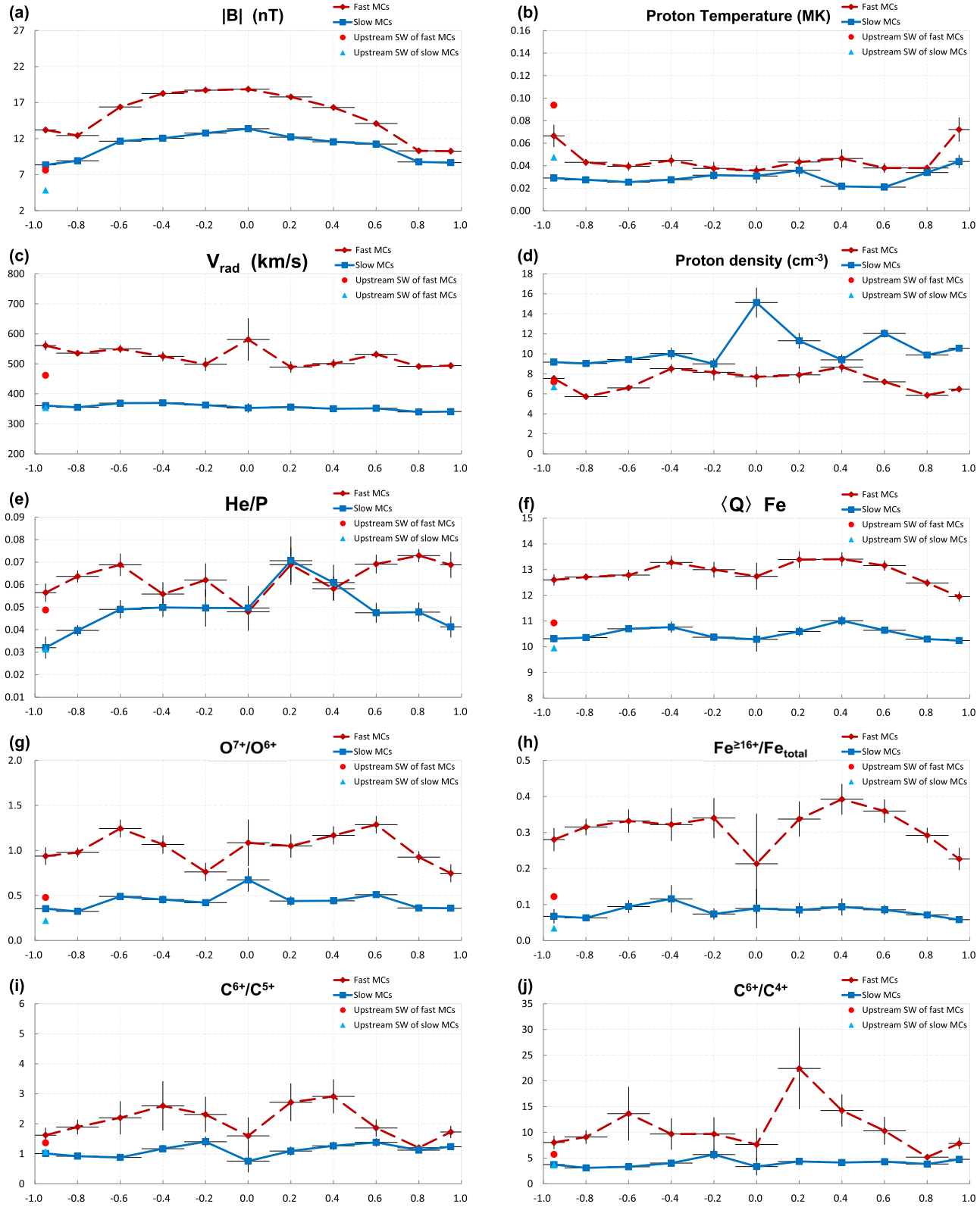

Figure 3. Statistical distributions of plasma and composition inside MCs by *ACE* in 1998–2011. The red dashed lines are the quantity distributions inside fast MCs. The blue curves denote the quantity distributions inside slow MCs. Error bars represent the standard error of the mean in each bin. The red dots denote upstream SW mean value of fast MCs, the blue triangles denote the upstream SW mean value of slow MCs. Note that the edge bins span −1.0 to −0.9 and 0.9 to 1.0, respectively.

the altitude far from the Sun (e.g., $Fe^{8+} \sim Fe^{12+}$ freeze-in $1.3 \sim 2.1\ R_{\odot}$ (Chen et al. 2003)), thus they are sensitive to continuing heating in extended space. The most reliable indicator of Fe charge state behavior is $\langle Q \rangle$Fe (Lepri & Zurbuchen 2004), providing an identifier of heating experience independent of expansion processes and heliocentric distance. Fast MCs have an apparently higher value than slow ones in $\langle Q \rangle$Fe, as well as upstream SW. Both fast and slow MCs have a bimodal

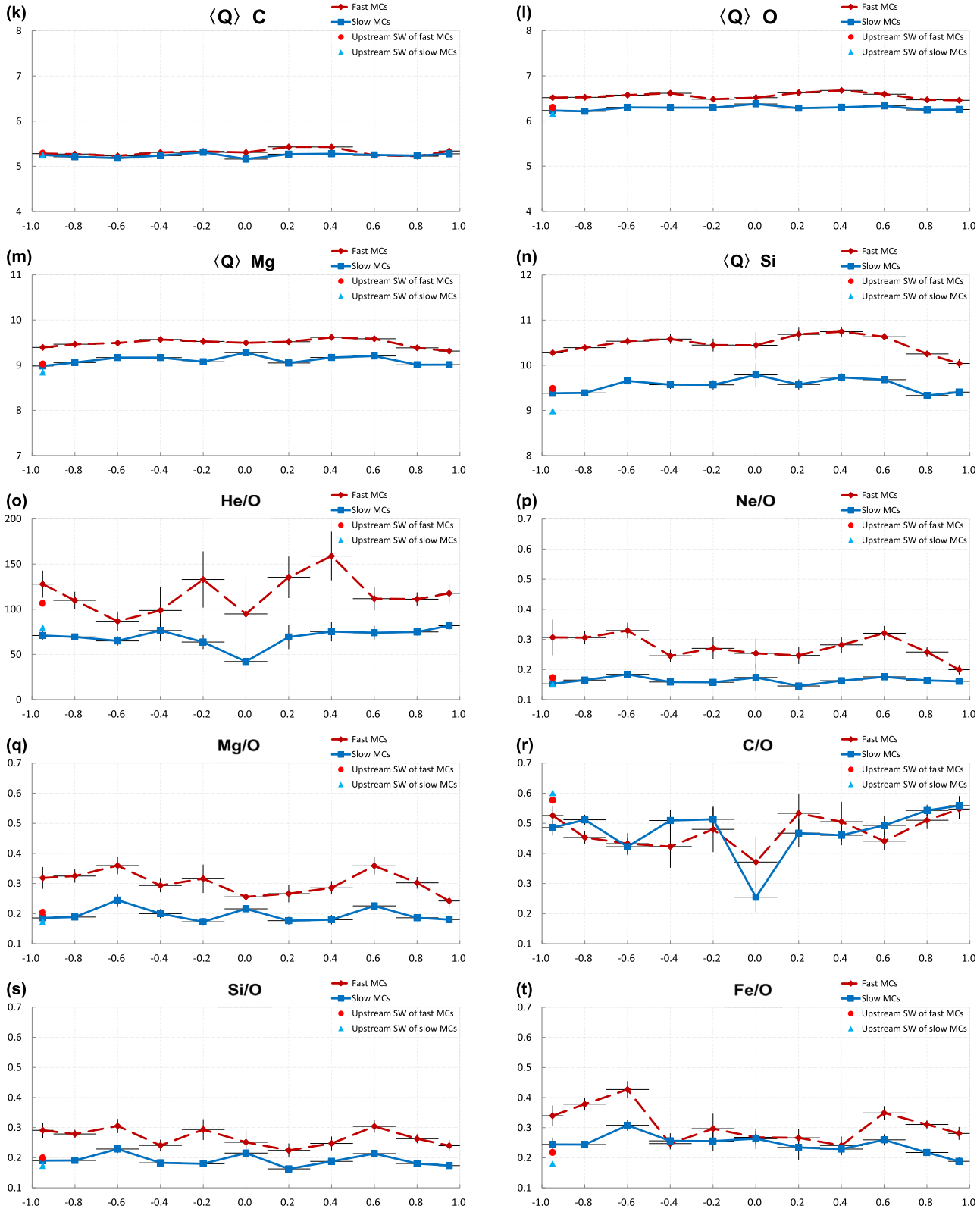

Figure 3. (Continued.)

distribution, the peaks are symmetrically distributed at $x = \pm 0.4$, and posterior peaks (13.40 for fast MCs, 11.01 for slow MCs) are slightly higher than those of the anterior ones (13.28 for fast MCs, 10.76 for slow MCs).

(g) O^{7+}/O^{6+} ratio. Since the dominant ions of oxygen, i.e., O^{6+} and O^{7+}, freeze-in 1.0 ~1.9 $R_{\odot}$ (Chen et al. 2003), O^{7+}/O^{6+} ratio is one of the diagnostics of low corona temperature. Panel (g) shows that fast MCs exhibit general

bimodality in O^{7+}/O^{6+}, but slow MCs distribution profile tends to be uniform.

(h) $Fe^{\geqslant 16+}/Fe_{total}$ ratio. The high iron charge states $Fe^{\geqslant 16+}$ (at least Fe XVII) representative of the materials heated by solar flares, with electron temperatures of up to 10 ~20 MK (Lepri & Zurbuchen 2004). Panel (h) shows that the enhancement of $Fe^{\geqslant 16+}$ within fast MCs is fairly pronounced, as well as the bimodality and further enhancement of posterior peak, whereas the distribution of slow MCs is nearly flat and there is no obvious posterior peak.

(j) and (i) C^{6+}/C^{4+} and C^{6+}/C^{5+} ratio. All of them are indicators of the thermal environment in the source. The main carbon ionization states C^{4+}, C^{5+}, and C^{6+} freeze-in $1.16 \sim 1.26\ R_{\odot}$ (Chen et al. 2003), which is a relatively well-defined radial range compared to oxygen (Landi et al. 2012). They also exhibit bimodality for both fast and slow MCs, though C^{6+}/C^{4+} of slow MCs does not show obviously.

(k)–(n) Mean charge state distributions of carbon $\langle Q\rangle$C, oxygen $\langle Q\rangle$O, magnesium $\langle Q\rangle$Mg, and silicon $\langle Q\rangle$Si, respectively. Their profiles are not exactly the same. $\langle Q\rangle$O and $\langle Q\rangle$Si profiles show similar bimodal distributions to $\langle Q\rangle$Fe, but the other two do not have such characteristics. This is because different elements correspond to different freeze-in altitudes; therefore, some of them are not affected by continuing heating along with a more extended space like Fe ions (e.g., Ko et al. 2010; Gruesbeck et al. 2011; Lepri et al. 2012). In addition, combining panels (f) and (k)–(n) and considering the elements atomic number allowed an increase in mean charge state with the atomic number to be seen, which agree with characteristics in the solar wind and ICMEs (e.g., Ko et al. 1999; Gruesbeck et al. 2012; Landi et al. 2012). Furthermore, if we sort the mean charge state of ions by the size of the difference between fast and slow MCs, that is $\langle Q\rangle$Fe $>$ $\langle Q\rangle$Si $>$ $\langle Q\ \rangle$Mg $>$ $\langle Q\rangle$O $>$ $\langle Q\rangle$C. The order is also the same as the atomic number of elements from large to small. The cause is probably that the ions of the higher atomic numbers are easier to ionize to higher charge state by electron collisions or by direct heating.

(o)–(t) Elemental abundance of He, Ne, Mg, C, Si, and Fe relative to O respectively. Dominated by first ionization potential (FIP) fractionation or mass fractionation, they are calculated by summing over all charge states of each element. Compared with upstream SW, Mg/O, Si/O, and Fe/O in fast MCs exhibit abundance increase, all of them are low-FIP (FIP $\leqslant$ 10 eV) elements relative to O. On the other hand, for high-FIP elements relative to O, Ne/O of fast MCs also shows significant enhancement, He/O shows less enhancement than upstream SW, while C/O shows apparent depletion. These characteristics of fast MCs are coincident with ICMEs explained by FIP fractionation (Zurbuchen et al. 2016). Besides, the slow MCs' elemental abundances are close to upstream SW, but much lower than fast MCs, which are either due to the intensive FIP effect that the pre-CME material of fast CME has experienced (different FIP effect implying different chromospheric structure or processes; Geiss et al. 1995), or should be understood by mass fractionation (Wurz et al. 2000).

These results show that the magnetic field, plasma, and ionic composition distribution profiles inside fast and slow MCs appear in similarities and differences. In general, fast MCs tend to be enhanced and more fluctuant than slow ones.

5. Discussion and Conclusions

In this study, we present the statistical plasma and composition distribution inside fast and slow MCs, respectively, including He/P ratio, proton density, the magnetic field magnitude, proton temperature, average radial velocity, heavy-ion charge state of Fe, O, Si, Mg, and O^{7+}/O^{6+}, $Fe^{\geqslant 16+}/Fe_{total}$, C^{6+}/C^{4+}, and C^{6+}/C^{5+} ratios, as well as elemental abundance ratios of Ne/O, Mg/O, Si/O, C/O, and He/O. Our results indicate that the MCs have specific structures with statistical features in the plasma and composition quantities. The interior of fast MCs has enhanced ionic charge state distributions more than slow ones, which should be attributed to the fact that the origin of a heated coronal environment contains more energy at 1 au. By comparing such enhancement of fast MCs for elemental species, an increase in the enhancement with atomic number is found. Additionally, for the distribution profiles, fast MCs are similar to slow MCs in the striking bimodality shown in $\langle Q\rangle$Fe, $Fe^{\geqslant 16+}/Fe_{total}$, and C^{6+}/C^{4+} distributions. The difference is that the posterior peak of fast MCs is slightly higher than the anterior one, whereas two peaks are comparable in fast MCs. To the best of our knowledge, this is an unprecedented finding.

$\langle Q\rangle$Fe are good indications of coronal electron temperature (Lynch et al. 2003). A bimodal distribution of $\langle Q\rangle$Fe inside MCs indicates that the measured MCs contain a low ionized center and high ionized shell. Song et al. (2016) consider that high temperature current sheet generates high charge state Fe ions, and fill in the corresponding layers of the flux rope, which may have been formed prior to the eruptions. In our statistics, bimodality is found in $\langle Q\rangle$Fe distributions inside both fast and slow MCs, implying that preexisting flux rope is likely to be more common than we expected.

It is noteworthy that for the bimodal distribution of $\langle Q\rangle$Fe inside fast MCs, the peak close to the Sun is higher than the other one. $Fe^{\geqslant 16+}/Fe_{total}$, O^{7+}/O^{6+}, and C^{6+}/C^{4+} also have similar characteristics. The possible cause is that the rear of fast flux rope CME faces the Sun. Based on the "standard model" for CME/flares (Lin & Forbes 2000; Hudson & Cliver 2001), when an eruption happens, the sunward side of the flux rope connects to the current sheet, where electrons are accelerated and flow out into the rising flux rope subsequently. The electron beam is capable of ionizing surrounding material by collisions (Miller & Vinas 1993). The sunward side flux rope ions get more high-energy electron collisions and would therefore elevate to higher charge states than the opposite side. Our results are also consistent with the previous observational study. Yan et al. (2018) analyzed an eruptive flare associated with a fast flux rope CME event using *SDO*/AIA data. As the temperature maps derived from the differential emission measure showed (see Figure 4 in Yan et al. 2018), there is a hot ring region inside the flux rope during the eruption, and the bottom of the ring is hotter than the other regions. However, for slow MCs, the two peaks are comparable, possibly because most slow MCs' counterparts are quiescent filament eruptions without flares.

Wang et al. (2016) and Zhao et al. (2017) found that some MCs had a significant propagation velocity perpendicular to the radial direction, suggesting direct evidence of the CME rotation in interplanetary space, and they inferred that a significant poloidal motion did exist in some MCs. Considering that the two peaks inside ionic charge state distribution of fast MCs are different in our statistics, it is likely that the propagation time of

fast MCs in the interplanetary space is not enough to balance the ions in the front and rear before they are observed at 1 au. Alternatively, the proportion of such poloidal motion in fast MCs is possibly too small to affect statistical results.

What determines the velocities of CMEs is still a question. In our explanation for the bimodal distribution of charge state inside MCs, magnetic reconnection is absolutely necessary. To be specific, the high-energy electron collisions of reconnection outflow cause a quite similar bimodality in $\langle Q \rangle$Fe distribution inside both fast and slow MCs. On the other hand, the ionic charge states of fast MCs are significantly higher than slow MCs, which means that the electron collisions and flare direct heating on the source region of fast CMEs are more pronounced with a higher reconnection participation level. This finding is in correspondence with the view of Qiu & Yurchyshyn (2005) that CME velocities are proportional to the total reconnection flux estimated from the flare brightened region and extrapolation magnetic fields. It is reasonable that faster CME corresponds to the larger flare brightened region, which means that more fluxes are involved in the reconnection, causing higher energy electron collisions or higher temperature heating, then resulting in enhanced ionic charge state.

Finally, it is worth noting that our statistical results were based on the spatial structure which is derived from the application of the static, cylindrical, linear, force-free magnetic field model. Although this model was applied successfully to case studies and reproduced the general magnetic structure of the flux rope to some extent, it is based on some assumptions. Non-force-free fields, elliptical cross-section shape, and/or torus-shaped flux rope model may be closer to reality. Nevertheless, as commented on by Lynch03, complicated models bring diverse physical geometry of the flux rope, and it is difficult to construct an average profile with multiple events and perform statistic analysis.

This work is funded by the grants from the Strategic Priority Research Program of CAS with grant XDA-17040507, and the National Science Foundation of China (NSFC 11533009, 11973086). This work is also funded by the Project Supported by the Specialized Research Fund for Shandong Provincial Key Laboratory. In addition, we are also grateful to the One Belt and One Road Scientific Project of the West Light Foundation, CAS. The authors Y.L. and Z.Z.A. would like to thank the University of Malaya Faculty of Science grant (GPF040B-2018) for support. All the *ACE* and *WIND* data are from NASA CDAWeb. We are grateful to the data provided by the NASA/GSFC. We are also grateful to the magnetic flux ropes list created by the Solar and Space Weather Research Group, Korea Astronomy and Space Science Institute. One of the authors, J.H., would like to thank Prof. Ilia Roussev for his stimulating discussion. Anonymous reviewer and editors' comments that were valuable for improving our manuscript are acknowledged.

ORCID iDs

Jin Huang https://orcid.org/0000-0003-0099-0406
Yu Liu https://orcid.org/0000-0002-7694-2454
Hengqiang Feng https://orcid.org/0000-0003-2632-8066
Ake Zhao https://orcid.org/0000-0002-6740-2659
Yuandeng Shen https://orcid.org/0000-0001-9493-4418

References

Bemporad, A., Poletto, G., Suess, S. T., et al. 2006, ApJ, 638, 1110
Bothmer, V., & Schwenn, R. 1998, AnGeo, 16, 1
Burlaga, L., Sittler, E., Mariani, F., et al. 1981, JGR, 86, 6673
Burlaga, L. F. 1988, JGR, 93, 7217
Burlaga, L. F., Klein, L., Sheeley, N. R., et al. 1982, GeoRL, 9, 1317
Burlaga, L. F., Skoug, R. M., Smith, C. W., et al. 2001, JGR, 106, 20957
Chen, A. Q., Chen, P. F., & Fang, C. 2006, A&A, 456, 1153
Chen, J. 1996, JGR, 101, 27499
Chen, Y., Esser, R., & Hu, Y. 2003, ApJ, 582, 467
Cheng, X., Ding, M. D., Zhang, J., et al. 2014a, ApJ, 789, 93
Cheng, X., Zhang, J., Ding, M. D., et al. 2013, ApJ, 763, 43
Chiu, M. C., von-Mehlem, U. I., Willey, C. E., et al. 1998, SSRv, 86, 257
Ciaravella, A., Webb, D. F., Giordano, S., & Raymond, J. C. 2013, ApJ, 766, 65
Elliott, H. A., McComas, D. J., Schwadron, N. A., et al. 2005, JGRA, 110, A04103
Geiss, J., Gloeckler, G., von Steiger, R., et al. 1995, Sci, 268, 1033
Gibson, S. E., & Low, B. C. 1998, ApJ, 493, 460
Gloeckler, G., Cain, J., Ipavich, F. M., et al. 1998, SSRv, 86, 497
Gosling, J. T. 1990, GMS, 58, 343
Gosling, J. T., Eriksson, S., McComas, D. J., et al. 2007, JGRA, 112, A08106
Gruesbeck, J. R., Lepri, S. T., Zurbuchen, T. H., et al. 2011, ApJ, 730, 103
Gruesbeck, J. R., Lepri, S. T., & Zurbuchen, T. H. 2012, ApJ, 760, 141
Howard, T. A. 2011, JASTP, 73, 1242
Hu, Q., & Sonnerup, B. U. Ö 2002, JGRA, 107, 1142
Hudson, H. S., & Cliver, E. W. 2001, JGR, 106, 25199
Kim, R.-S., Gopalswamy, N., Cho, K.-S., et al. 2013, SoPh, 284, 77
Klein, L. W., & Burlaga, L. F. 1982, JGR, 87, 613
Ko, Y.-K., Gloeckler, G., Cohen, C. M. S., et al. 1999, JGR, 104, 17005
Ko, Y.-K., Raymond, J. C., Rakowski, C., & Rouillard, A. 2013, in AIP Conf. Proc. 1539, Solar Wind 13, ed. G. P. Zank et al. (Melville, NY: AIP), 207
Ko, Y.-K., Raymond, J. C., Vršnak, B., et al. 2010, ApJ, 722, 625
Landi, E., Alexander, R. L., Gruesbeck, J. R., et al. 2012, ApJ, 744, 100
Landi, E., Gruesbeck, J. R., Lepr, S. T., Zurbuchen, T. H., & Fisk, L. A. 2012, ApJ, 761, 48
Lepping, R. P., Berdichevsky, D. B., Wu, C.-C., et al. 2006, AnGeo, 24, 215
Lepping, R. P., Jones, J. A., & Burlaga, L. F. 1990, JGR, 95, 11957
Lepping, R. P., Wu, C.-C., Berdichevsky, D. B., et al. 2011, SoPh, 274, 345
Lepri, S. T., Laming, J. M., Rakowski, C. E., & von Steiger, R. 2012, ApJ, 760, 105
Lepri, S. T., & Zurbuchen, T. H. 2004, JGRA, 109, A01112
Lin, J., & Forbes, T. G. 2000, JGR, 105, 2375
Lin, J., Raymond, J. C., & van Ballegooijen, A. A. 2004, ApJ, 602, 422
Lindsay, G. M., Luhmann, J. G., Russell, C. T., & Gosling, J. T. 1999, JGR, 104, 12515
Liu, Y., Jiang, Y., Ji, H., et al. 2003, ApJL, 593, L137
Lugaz, N., Manchester, W. B., & Gombosi, T. I. 2005, ApJ, 634, 651
Lugaz, N., & Roussev, I. I. 2011, JASTP, 73, 1187
Lundquist, S. 1950, Ark. Fys., Stockholm 2, 35, 361
Lynch, B. J., Reinard, A. A., Mulligan, T., et al. 2011, ApJ, 740, 112
Lynch, B. J., Zurbuchen, T. H., Fisk, L. A., et al. 2003, JGRA, 108, 1239
McComas, D. J., Bame, S. J., Barker, P., et al. 1998, SSRv, 86, 563
Mikic, Z., & Linker, J. A. 1994, ApJ, 430, 898
Miller, J. A., & Vinas, A. F. 1993, ApJ, 412, 386
Neugebauer, M., & Goldstein, R. 1997, GMS, 99, 245
Osherovich, V. A., Farrugia, C. J., & Burlaga, L. F. 1993, AdSpR, 13, 57
Ouyang, Y., Yang, K., & Chen, P. F. 2015, ApJ, 815, 72
Owens, M. J. 2018, SoPh, 293, 122
Patsourakos, S., Vourlidas, A., & Stenborg, G. 2013, ApJ, 764, 125
Qiu, J., & Yurchyshyn, V. B. 2005, ApJL, 634, L121
Reinard, A. A., & Biesecker, D. A. 2009, ApJ, 705, 914
Richardson, I. G., & Cane, H. V. 2004, JGRA, 109, A09104
Rodriguez, L., Woch, J., Krupp, N., et al. 2004, JGRA, 109, A01108
Smith, C. W., L'Heureux, J., Ness, N. F., et al. 1998, SSRv, 86, 613
Song, H. Q., Chen, Y., Zhang, J., et al. 2015a, ApJL, 804, L38
Song, H. Q., Chen, Y., Zhang, J., et al. 2015b, ApJL, 808, L15
Song, H. Q., Zhang, J., Chen, Y., et al. 2015c, ApJ, 803, 96
Song, H. Q., Zhang, J., Cheng, X., et al. 2014, ApJ, 784, 48
Song, H. Q., Zhong, Z., Chen, Y., et al. 2016, ApJS, 224, 27
Vršnak, B., Sudar, D., & Ružđjak, D. 2005, A&A, 435, 1149
Wang, Y., Shen, C., Liu, R., et al. 2018, JGRA, 123, 3238
Wang, Y., Zhuang, B., Hu, Q., et al. 2016, JGRA, 121, 9316

Wurz, P., Bochsler, P., & Lee, M. A. 2000, JGR, 105, 27239
Yan, X. L., Yang, L. H., Xue, Z. K., et al. 2018, ApJL, 853, L18
Yashiro, S., Gopalswamy, N., Michalek, G., & Howard, R. A. 2002, BAAS, 34, 695
Zhang, J., Cheng, X., & Ding, M.-D. 2012, NatCo, 3, 747
Zhao, A., Wang, Y., Liu, J., et al. 2017, ApJ, 845, 109
Zurbuchen, T. H., Fisk, L. A., Lepri, S. T., et al. 2003, in AIP Conf. Proc. 679, Solar Wind 10, ed. M. Velli et al. (Melville, NY: AIP), 604
Zurbuchen, T. H., & Richardson, I. G. 2006, SSRv, 123, 31
Zurbuchen, T. H., Weberg, M., von Steiger, R., et al. 2016, ApJ, 826, 10